Bilateral Inertia and Damping Emulation Control Scheme of VSC-HVDC Transmission Systems for Asynchronous Grid Interconnections

Jiebei Zhu, *Senior Member, IEEE*, Zhipeng Shen, *Student Member, IEEE*, Lujie Yu, Siqi Bu, *Senior Member, IEEE*, Xialin Li, *Member, IEEE*, Chi Yung Chung, *Fellow, IEEE*, Campbell Booth, Hongjie Jia, *Senior Member, IEEE*, Chengshan Wang, *Senior Member, IEEE*

***Abstract*—This paper proposes a novel bilateral inertia and damping emulation (BIDE) control scheme for VSC-HVDC transmission systems that can autonomously provide inertial and damping responses to two VSC-HVDC interconnected asynchronous AC grids in a similar fashion of synchronous generators. For each VSC station, the energy for inertia emulation comes from augmented DC link capacitance whereas the energy for damping emulation comes from the interconnected grid on the other side. This proposed approach is communication-free as the essential information of two grid frequencies for inertia and damping emulation can be obtained from the locally measured variables dictated by the BIDE control algorithms. Modal analysis is carried out to investigate the impacts of BIDE-emulated inertia time constants and damping factors on system small-signal stability, and to obtain the optimal control parameters. The effectiveness of the proposed BIDE scheme is verified through controller hardware-in-the-loop experiments, in the presence of load changes and grid faults. The results show that the BIDE scheme can effectively enhance the stability and damp the frequency oscillations for both AC grids.**

***Index Terms*—Frequency response, HVDC transmission control, pulse width modulated power converters, power system transients, frequency stability.**

I. Introduction

WITH the rapid development of renewable energy sources (RESs) in modern power systems, there is an increasing trend for interconnecting asynchronous grids via VSC-HVDC systems to mitigate the power imbalances incurred by the RES volatility and meet the incremental demand engendered by the electricity transactions, such as UK-Ireland interconnection [1] and Nortctheast Asia grid interconneion [2]. However, unlike conventional AC grids which enable power synchronization between the asynchronous systems, the VSC-HVDC transmission systems under the traditional control deny this synchronous power supports, meaning that the kinetic inertia and spinning reserves available in each asynchronous grid cannot be mutually shared [3]. In addition, inertia- and damping-less RESs, which are rapidly replacing grid-friendly synchronous generators (SGs), is further lowering the grid inertia levels and damping effects. Therefore, the grid frequency stability is inevitably compromised.

When a grid experiences certain contingency (e.g. grid faults), the inertia of a generator rotor restricts the grid Rate of Change of Frequency (RoCoF), meanwhile the damping windings of a generator rotor apply an effective stabilizing impact on the rotor angle variations. Recent blackouts in Australia and the UK indicate the deterioration of existing grid frequency regulations and the increased demand for competent frequency control schemes, such as inertia and damping control (IDEC), for low-inertia power grids [4], [5].

To address the low-inertia related issues, many advanced control approaches have been proposed for RESs. As reported in [6], a wind turbine generator operates on a power de-loaded mode through pitch control to keep certain power reserve for frequency support. Similarly, in [7], photovoltaic is suggested to work at sub-optimal voltage potentials. These strategies, however, are economically unjustified, as the power reserve is wasted for most of time. In [8], a synthetic inertia control for doubly fed induction generator is proposed using super-capacitors, which avoids power reserve losses due to de-loading. However, from the perspective of transmission grid operation, the system inertia segmentation issue caused by VSC-HVDC links blocks the RES synthetic inertia for the VSC-HVDC interconnected remote asynchronous grids, posing a major challenge for the planning and operation of future RES-dense power grids.

Generally, for a point-to-point VSC-HVDC system under TC, as illustrated in Fig. 1, one converter acts as a power-regulating VSC (PR-VSC) and the other one as a DC-voltage-regulating VSC (VR-VSC). Under TC, neither RP-VSC nor VR-VSC contributes inertia provision for their connected AC grids, as indicated in Fig. 2(a). Historically reported inertia and damping emulation schemes for VSC-HVDC systems can be classified according to the types of energy sources: energy from the remote side of a VSC-HVDC interconnected AC grid (e.g. IDEC schemes in [9]–[19]) or from DC capacitors (e.g. coordinated inertia and damping emulation control (CIDE) schemes in [20]–[25]) .

1) The IDEC schemes, as shown in Fig. 2(b). The PR-VSC for AC Grid P utilizes energy for the IDEC solely from AC Grid V via the VSC-HVDC link. A power-synchronization control is proposed in [9], in which the phase-lock loop (PLL) is substituted by an active power synchronization loop to emulate an SG. Virtual synchronous generator or machine (VSG or VSM) schemes are reported in [10]–[13] to allow the VSCs to mimic the SGs' inertial and damping behaviors, but the output current exhibits high-frequency ripples that potentially affect transient stability [14]. References [14]–[16] insert an

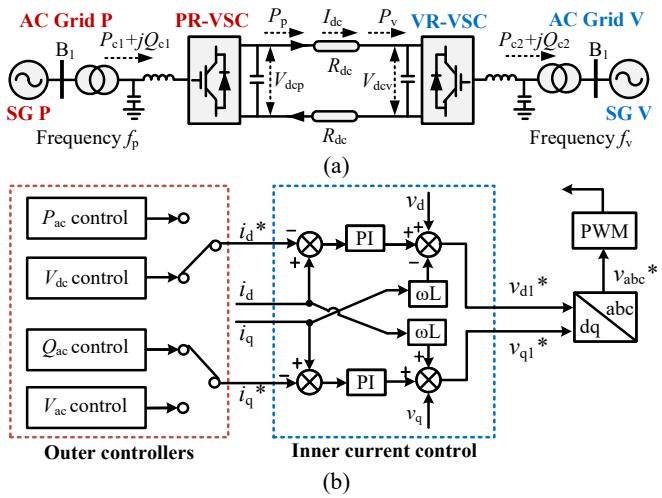

Fig. 1. Single-line diagram of a VSC-HVDC transmission system: (a) configuration of the VSC-HVDC system; and (b) traditional control scheme.

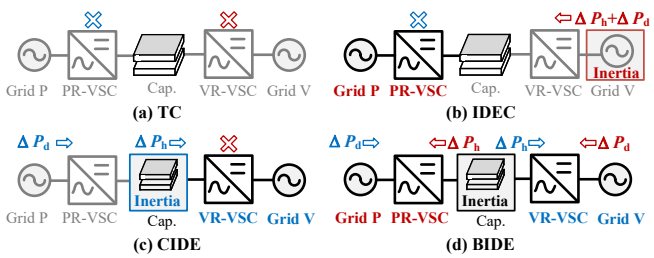

Fig. 2. The power flow diagrams of four control schemes where ΔP_h represents inertial power provision and ΔP_d represents damping power provision: (a) TC scheme; (b) IDEC scheme; (c) CIDE scheme; and (d) BIDE scheme.

additional synchronous power controller in a virtual admittance structure design to reduce the current ripples. References [17] and [18] demonstrate that the provision of inertia support from an OWF via VSC-HVDC is feasible. However, the schemes in [9]–[18] can only provide the inertial and damping support to one side.

To avoid this issue, a novel control scheme is proposed in [19] to provide the mutual inertial support based on the priority selection unit. However, such a priority selection unit requires minimum service durations to avoid frequent priority switching, reducing the activating sensitivity of the bilateral inertial response. Besides, the inertial support can only be provided to one asynchronous grid at one time determined by the priority selection unit. More importantly, all the schemes in [9]–[19] require rapid power run-up or run-down from the healthy-AC grid connected converter station to support the faulted or disturbed AC grid, which in fact propagates such faults or disturbances to the healthy-AC grid. Therefore, these schemes cannot provide "incremental" inertial response considering both AC grids.

2) **The CIDE schemes, as shown in Fig. 2(c).** Another inertia emulation control (INEC) scheme is developed for VSC-HVDC system in [20], [21], leveraging the energy in the DC capacitors to emulate inertia time constant by varying the DC voltage, while the AC grid connected on the other side is not affected. Nevertheless, the INEC scheme does not mimic the SG damping characteristics which can effectively suppress angular oscillations as designed in [10]. Other CIDE schemes, as proposed in [22]–[25], use both the energy of the DC capacitors and the kinetic energy of wind turbines to provide the inertial response. However, the CIDE schemes in [20]–[25] are not designed to provide frequency support to OWF systems under offshore grid contingencies.

To enable the VSC-HVDC inertial and damping responses simultaneously to both interconnected AC grids, this paper proposes a novel bilateral inertia and damping emulation (BIDE) control scheme as shown in Fig. 2(d). The main contributions of this paper are summarized as follows

1) Unlike the inertia emulation control in [9]–[25], the proposed BIDE scheme can emulate SG inertial responses for two AC grids interconnected via a VSC-HVDC link. The inertial power for either side grid comes from the augmented DC link capacitance, avoiding the disturbance to both AC grids.

2) The proposed BIDE scheme can emulate flexibly-defined SG damping factors for both AC grids, using the active power from the other side of the interconnected asynchronous grid.

3) Unlike the emulation scheme in [19] which uses the priority selection control, the proposed BIDE scheme can "simultaneously" provide the inertial and damping support to both connected asynchronous grids, avoiding the disturbing mode switching actions.

4) The approach is communication-free for the essential frequency information acquisition of the remote grid, improving control reliability and avoiding control latency.

The rest of this paper is organized as follows. The VSC-HVDC system configuration is briefly introduced and its power flow is analyzed in Section II. Section III presents the mathematical algorithm and controller implementation of the proposed BIDE scheme. In Section IV, the small-signal stability analysis of the BIDE scheme is carried out. Section V verifies the effectiveness of the proposed BIDE scheme through controller hardware-in-the-loop (C-HIL) experiments. Finally, Section VI draws conclusions.

II. VSC-HVDC System Configuration and Power Flow Analysis

A. VSC-HVDC configuration and traditional control

Fig. 1(a) illustrates a typical point-to-point configuration of a VSC-HVDC system, interconnecting AC Grid P and V. Two VSC converters are operated with their local control systems to realize bidirectional power transmission and DC voltage regulation, respectively. For each VSC converter, AC phase reactor and shunt filter are used to attenuate high-order harmonics.

TC scheme for VSC-HVDC systems is generally designed in a cascaded structure, as illustrated in Fig. 1(b). The AC current at the point of common coupling (PCC) is controlled by an inner current loop to compute converter voltage reference for pulse width modulation (PWM). A phase lock loop (PLL) is used to track grid voltage angular phase θ at the PCC to ensure the synchronization of the VSC with the grid. The active and reactive power are independently controlled by outer power loops. Otherwise, the DC voltage is regulated by an outer DC voltage control loop for DC network power balance.

Regulating the AC voltage can be realized by an outer AC voltage control instead of outer reactive power control. The detailed VSC-HVDC control parameter design of TC has been well documented in [9].

B. Power flow analysis of the VSC-HVDC systems

As the communication-less feature of the proposed BIDE is based on the locally measured variables of the VSC-HVDC systems, the power flow analysis of the VSC-HVDC system is conducted for the further control design. As illustrated in Fig. 1(a), $P_{\rm p}$ and $P_{\rm v}$ are the injected and received active power of PR-VSC and VR-VSC, respectively, $V_{\rm dcp}$ and $V_{\rm dcv}$ are the DC terminal voltages of PR-VSC and VR-VSC, respectively, and $I_{\rm dc}$ and $R_{\rm dc}$ are the DC current and equivalent DC resistance of the DC cables, respectively. The DC-side electrical characteristics of the VSC-HVDC system can be described as

$$\begin{cases} V_{\rm dcp} = V_{\rm dcv} + 2I_{\rm dc}R_{\rm dc} \\ P_{\rm p} = V_{\rm dcp}I_{\rm dc} \\ P_{\rm v} = V_{\rm dcv}I_{\rm dc} \end{cases} \tag{1}$$

According to (1), the PR-VSC injected active power can be rewritten as

$$P_{\rm p}=\left(V_{\rm dcv} + 2I_{\rm dc}R_{\rm dc}\right)I_{\rm dc} \tag{2}$$

Based on (1) and (2), the DC current $I_{\rm dc}$ can be expressed as

$$I_{\rm dc}=\frac{V_{\rm dcv}}{4R_{\rm dc}}\left(-1+\sqrt{1+\frac{8P_{\rm p}R_{\rm dc}}{V_{\rm dcv}^2}}\right) \tag{3}$$

According to (1) and (3), the DC voltage $V_{\rm dcp}$ can be calculated as

$$V_{\rm dcp} = \frac{V_{\rm dcv}}{2}\left(1+\sqrt{1+\frac{8P_{\rm p}R_{\rm dc}}{V_{\rm dcv}^2}}\right) \tag{4}$$

As observed in (4), the DC voltage of PR-VSC $V_{\rm dcp}$ can be effectively estimated according to the VR-VSC DC voltage $V_{\rm dvc}$, the PR-VSC active power $P_{\rm p}$, and the DC resistance $R_{\rm dc}$. And it can be clearly found from (4) that the DC voltage can be used as an intermediary to transfer the frequency information from VR-VSC to PR-VSC as the PR-VSC voltage correspondingly varies along with the VR-VSC DC voltage change, which will be further used for the communication-free bilateral frequency acquisition as detailed in Section *III.D*.

III. Bilateral Inertia and Damping Emulation Control for VSC-HVDC Systems

A. The SG swing equation

The swing equation of an SG [26] is expressed as

$$\frac{2H_{\rm sg}}{f_0}\frac{df}{dt} + D_{\rm sg}\frac{(f-f_0)}{f_0} = P_{\rm m} - P_{\rm e} \tag{5}$$

where $H_{\rm sg}$ and $D_{\rm sg}$ are the emulated inertia time constant and damping factor of the SG in seconds and in pu, respectively; f and f_0 refer to the instantaneous and nominal frequency in Hz, respectively; and $P_{\rm m}$ and $P_{\rm e}$ are the input mechanical and output electrical power in pu, respectively.

According to (5) , the SG inertial power $\Delta P_{\rm h}$ and damping power$\Delta P_{\rm d}$ can be expressed as

$$\Delta P_{\rm h} = \frac{2H_{\rm sg}}{f_0}\frac{df}{dt} \tag{6}$$

$$\Delta P_{\rm d} = D_{\rm sg}\frac{f-f_0}{f_0} \tag{7}$$

In (6) and (7): 1) an SG's inertial power exchange with the grid is proportional to the grid RoCoF *df/dt*, and vanishes to 0 after reaching to steady states; 2) an SG's inherent damping power is proportional to the frequency deviation from a nominal value (f - f_0), and is induced whenever any frequency variation exists.

B. Inertia emulation by BIDE

The CIDE scheme as reported in [20] utilizing the energy stored in the DC capacitance of the VSC-HVDC provides the inertial power only to the VR-VSC connected AC grid. As a significant improvement over CIDE, the proposed BIDE in this paper aims to provide inertial responses bilaterally to both the VR-VSC connected and PR-VSC connected asynchronous grids, using capacitance energy without affecting the remote VSC-HVDC interconnected grid. The development of the BIDE inertia emulation algorithm is presented as follows.

According to (6), the total inertial power considering the frequencies of both grids can be expressed as

$$\Delta P_{\rm hpv} = \Delta P_{\rm hp} + \Delta P_{\rm hv} = \frac{2H_{\rm vscp}}{f_0}\frac{df_{\rm p}}{dt} + \frac{2H_{\rm vscv}}{f_0}\frac{df_{\rm v}}{dt} \tag{8}$$

where $\Delta P_{\rm hpv}$ is the inertial power provided to both AC grids in pu; $\Delta P_{\rm hp}$ and $\Delta P_{\rm hv}$ are the inertial powers provided to the PR-VSC and VR-VSC in pu, respectively; $H_{\rm vscp}$ and $H_{\rm vscv}$ are the separately emulated inertia time constants for the PR-VSC and VR-VSC in seconds, respectively; and $f_{\rm p}$ and $f_{\rm v}$ represent the frequencies measured by the PLLs of PR-VSC and VR-VSC in Hz, respectively.

The power exchange of the DC capacitors $\Delta P_{\rm C}$ can be quantified by varying the DC voltage level via VR-VSC as

$$\Delta P_{\rm C} = \frac{NCV_{\rm dcv}}{S_{\rm vsc}}\cdot\frac{dV_{\rm dcv}}{dt} \tag{9}$$

where *N* is the total number of DC capacitors in the VSC-HVDC link; *C* is the capacitance of a single DC capacitor in farad; and $S_{\rm vsc}$ is the rated apparent power of a single VSC station in MVA.

Linking the inertial power $\Delta P_{\rm hpv}$ to the capacitance's electrostatic power $\Delta P_{\rm C}$ gives

$$\frac{2H_{\rm vscp}}{f_0}\frac{df_{\rm p}}{dt} + \frac{2H_{\rm vscv}}{f_0}\frac{df_{\rm v}}{dt} = \frac{NCV_{\rm dcv}}{S_{\rm vsc}}\cdot\frac{dV_{\rm dcv}}{dt} \tag{10}$$

The relationship between the frequencies of two asynchronous grids and the DC voltage of the VR-VSC is obtained after integrating both sides of (10) as

$$\int_{f_0}^{f_{\rm p}}\frac{2H_{\rm vscp}}{f_0}df_{\rm p} + \int_{f_0}^{f_{\rm v}}\frac{2H_{\rm vscv}}{f_0}df_{\rm v} = \int_{V_{\rm dcv0}}^{V_{\rm dcv}^*}\frac{NCV_{\rm dcv}}{S_{\rm vsc}}dV_{\rm dcv} \tag{11}$$

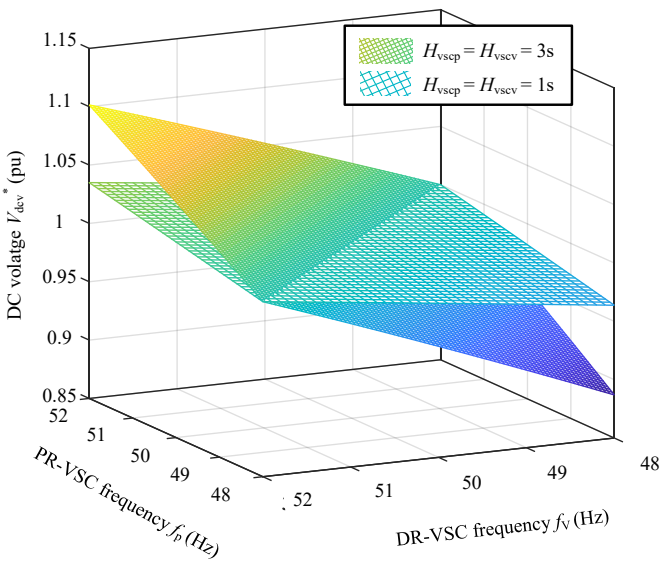

Fig. 3. The three-dimensional relationship of $V_{\mathrm{dcv}}^* - f_{\mathrm{p}} - f_{\mathrm{v}}$, where S_{vsc} = 300 MVA, N = 2, C = 7.5 mF, f_0 = 50 Hz and V_{dcv0} = 300 kV.

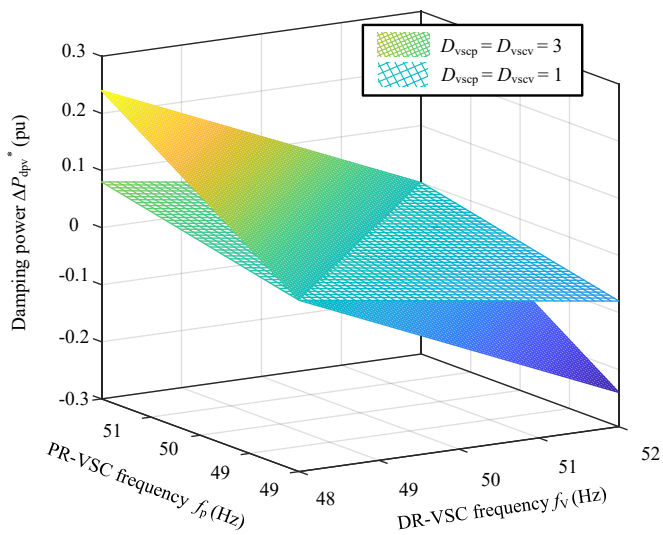

Fig. 4. The three-dimensional relationship of $\Delta P_{\mathrm{dpv}} - f_{\mathrm{p}} - f_{\mathrm{v}}$, where f_0 = 50 Hz.

$$V_{\mathrm{dcv}}^* = \sqrt{V_{\mathrm{dcv0}}^2 + \frac{4S_{\mathrm{vsc}}}{NCf_0}\left(H_{\mathrm{vscp}}\left(f_{\mathrm{p}} - f_0\right) + H_{\mathrm{vscv}}\left(f_{\mathrm{v}} - f_0\right)\right)} \quad (12)$$

where V_{dcv}^* and V_{dcv0} are the DC voltage reference and nominal DC voltage in kV, respectively.

Equation (12) indicates that, to emulate separated inertia time constant H_{vscp} and H_{vscv}, the DC voltage reference V_{dcv}^* should be dynamically coupled and positively correlated to the instantaneous PR-VSC frequency f_{p} and VR-VSC frequency f_{v}. Fig. 3 illustrates the three-dimensional relationship among the DC voltage $V_{\mathrm{dcv}}{}^*$ and the grid frequencies f_{p} and f_{v}. It can be seen that under the same frequency deviations, the DC voltage deviation increase with increased emulated inertia time constants.

Considering that the PR-VSC is directly controlled only to regulate the active power, the PR-VSC active power reference must operate in an immediate coordination with the VR-VSC DC voltage control, so as to deliver the required inertial power from the DC capacitance to AC Grid P as

$$P_{\mathrm{p1}}^* = P_{\mathrm{p0}} + \Delta P_{\mathrm{hp}} = P_{\mathrm{p0}} + \frac{2H_{\mathrm{vscp}}}{f_0}\frac{df_{\mathrm{p}}}{dt} \quad (13)$$

where P_{p0} and P_{p1}^* are the nominal and updated active power references of PR-VSC in pu, respectively. The positive sign in (13) indicates the power transmission direction from PR-VSC to VR-VSC.

C. Damping emulation by BIDE

The proposed BIDE also aims to mimic the SG damping effect to address potential grid angular oscillations in both AC grids or to the unnecessary power oscillations of both VSC stations themselves. Compared to the inertia emulation that accesses the DC capacitors' energy in the short term, as speculated in (7), the damping emulation requires incremental power continuously sustained in the relatively longer term when any frequency deviation exists. Therefore, the damping power to support one AC grid must be supplied from the remote AC grid interconnected by the VSC-HVDC system. The development of the BIDE damping emulation is presented as follows.

According to (7), the damping power provided to AC Grid P, ΔP_{dp}, can be expressed as

$$\Delta P_{\mathrm{dp}} = D_{\mathrm{vscp}}\frac{(f_{\mathrm{p}} - f_0)}{f_0} \quad (14)$$

where D_{vscp} is the emulated damping factor to AC Grid P via PR-VSC in pu.

Similarly, the damping power provided to AC Grid V, ΔP_{dv}, via VR-VSC can be expressed as

$$\Delta P_{\mathrm{dv}} = -D_{\mathrm{vscv}}\frac{(f_{\mathrm{v}} - f_0)}{f_0} \quad (15)$$

where D_{vscv} is the emulated damping factor of AC Grid V in pu. The negative sign in (15) indicates the power transmission direction is from PR-VSC to VR-VSC.

Combining the damping powers ΔP_{dp} and ΔP_{dv} gives the damping power provided to both AC grids, ΔP_{dpv}, as

$$\Delta P_{\mathrm{dpv}} = D_{\mathrm{vscp}}\frac{(f_{\mathrm{p}} - f_0)}{f_0} - D_{\mathrm{vscv}}\frac{(f_{\mathrm{v}} - f_0)}{f_0} \quad (16)$$

Equation (16) implies that providing the damping power for both AC grids requires the active power change to be controlled in proportion to both frequency deviations.

Fig. 4 shows the three-dimensional relationship of the damping power, ΔP_{dpv}, with the PR-VSC connected grid frequency, f_{p}, and the VR-VSC connected grid frequency, f_{v}. It can be observed that the damping power is linearly correlated with the difference between f_{p} and f_{v} under the same damping factors, effectively enabling the two AC grids to instantaneously share the overall power imbalance.

Considering the inertial power ΔP_{hp} in (13) and the damping power ΔP_{dpv} in (16), the PR-VSC active power reference under the proposed BIDE scheme is determined as

$$P_p^* = P_{\mathrm{p0}} + \Delta P_{\mathrm{hp}} + \Delta P_{\mathrm{dpv}} \quad (17)$$

$$P_{\mathrm{p}}^{*}=P_{\mathrm{p0}}+\frac{2H_{\mathrm{vscp}}}{f_0}\frac{df_{\mathrm{p}}}{dt}+D_{\mathrm{vscp}}\frac{(f_{\mathrm{p}}-f_0)}{f_0}-D_{\mathrm{vscv}}\frac{(f_{\mathrm{v}}-f_0)}{f_0} \quad (18)$$

where P_{p}^{*} is the RP-VSC active power reference in pu after emulating both the inertial and damping effects.

As the proposed BIDE scheme provides the inertial power to bilateral asynchronous AC grids only using the stored energy from the DC capacitance, the inertial power will not disturb the two interconnected asynchronous grids even though one of them is an island grid. As typical AC grids must have certain level of power reserve to guarantee the operational security, the effectiveness of the damping emulation will not be compromised as it only requires a minimum amount of the power reserve in one grid to support the other grid (only 0.01 pu active power variation as proved in a severe fault contingency in Section *V.C*).

D. Communication-free bilateral frequency acquisition

To implement the BIDE inertia and damping emulation as designed in Sections *III.B* and *III.C*, the instantaneous frequency information of AC Grid P for the remote VR-VSC control as in (12) and the instantaneous frequency information of AC Grid V for the remote PR-VSC control as in (18) must be identified. To acquire such frequency information, a communication-free approach is offered for the proposed BIDE, using the locally measured DC voltage or the active power, as further explained as follows.

1) Acquisition of AC Grid P frequency for VR-VSC: The VR-VSC active power change, ΔP_{v}, involves the power exchange of the DC system capacitance and the transmitted active power change of PR-VSC, expressed as

$$\Delta P_{\mathrm{v}}=\Delta P_{\mathrm{C}}-\Delta P_{\mathrm{p}} \quad (19)$$

where ΔP_{p} is the PR-VSC active power change in pu.

Based on (9) and (10), ΔP_{C} can be rewritten as

$$\Delta P_{\mathrm{C}}=\frac{2H_{\mathrm{vscp}}}{f_0}\frac{df_{\mathrm{p}}}{dt}+\frac{2H_{\mathrm{vscv}}}{f_0}\frac{df_{\mathrm{v}}}{dt} \quad (20)$$

Similarly, according to (18), ΔP_{p} can be expressed as

$$\Delta P_{\mathrm{p}}=\frac{2H_{\mathrm{vscp}}}{f_0}\frac{df_{\mathrm{p}}}{dt}+D_{\mathrm{vscp}}\frac{(f_{\mathrm{p}}-f_0)}{f_0}-D_{\mathrm{vscv}}\frac{(f_{\mathrm{v}}-f_0)}{f_0} \quad (21)$$

Combining (19) - (21), the active power change of VR-VSC, ΔP_{v}, can be expressed as

$$\Delta P_{\mathrm{v}}=\frac{2H_{\mathrm{vscv}}}{f_0}\frac{df_{\mathrm{v}}}{dt}-D_{\mathrm{vscp}}\frac{(f_{\mathrm{p}}-f_0)}{f_0}+D_{\mathrm{vscv}}\frac{(f_{\mathrm{v}}-f_0)}{f_0} \quad (22)$$

Based on (22), the frequency information of AC Grid P, f_{p}, can be estimated for the VR-VSC control based on its local measurement of AC Grid V frequency, f_{v}, and its power variation, ΔP_{v}, and the corresponding estimated frequency, f_{rp}, is expressed as

$$f_{\mathrm{rp}}=\left(1-\frac{\left(\Delta P_{\mathrm{v}}-\frac{2H_{\mathrm{vscv}}}{f_0}\frac{df_{\mathrm{v}}}{dt}-D_{\mathrm{vscv}}\frac{(f_{\mathrm{v}}-f_0)}{f_0}\right)}{D_{\mathrm{vscp}}}\right)f_0 \quad (23)$$

$$f_{\mathrm{rp}}-f_0=-\frac{f_0}{D_{\mathrm{vscp}}}\left(\Delta P_{\mathrm{v}}-\frac{2H_{\mathrm{vscv}}}{f_0}\frac{df_{\mathrm{v}}}{dt}-D_{\mathrm{vscv}}\frac{(f_{\mathrm{v}}-f_0)}{f_0}\right) \quad (24)$$

where the active power change ΔP_{v} in (23) can be calculated as

$$\Delta P_{\mathrm{v}}=P_{\mathrm{v}}-P_{\mathrm{v0}} \quad (25)$$

where P_{v0} is the VR-VSC instantaneous active power in steady state in pu, which is continuously measured before the occurrence of any disturbance.

Thus, with locally measured f_{v} and ΔP_{v}, the AC Grid P frequency information can be inferred in the VR-VSC control by (24) without communication.

2) Acquisition of AC Grid V frequency for PR-VSC: Similarly, the PR-VSC control can infer the instantaneous frequency information of AC Grid V via the DC voltage variations dictated by the VR-VSC inertia emulation. Based on (12), the relationship between the two grid frequencies and the VR-VSC terminal DC voltage can be rewritten as

$$\frac{H_{\mathrm{vscp}}\left(f_{\mathrm{p}}-f_0\right)+H_{\mathrm{vscv}}\left(f_{\mathrm{v}}-f_0\right)}{f_0}=\frac{NC}{4S_{\mathrm{vsc}}}\left(V_{\mathrm{dcv}}^2-V_{\mathrm{dcv0}}^2\right) \quad (26)$$

According to (4), the PR-VSC terminal DC voltage V_{dcp} can be derived from the VR-VSC terminal DC voltage V_{dcv} as

$$\begin{aligned}V_{\mathrm{dcp}}^2-V_{\mathrm{dcp0}}^2=&\left(\frac{V_{\mathrm{dcv}}}{2}\left(1+\sqrt{1+\frac{4P_{\mathrm{p}}R_{\mathrm{dc}}}{V_{\mathrm{dcv}}^2}}\right)\right)^2\\&-\left(\frac{V_{\mathrm{dcv0}}}{2}\left(1+\sqrt{1+\frac{4P_{\mathrm{p0}}R_{\mathrm{dc}}}{V_{\mathrm{dcv0}}^2}}\right)\right)^2\end{aligned} \quad (27)$$

where V_{dcp0} is the nominal PR-VSC terminal DC voltage and can be estimated by (4) in kV and V_{dcv0} is the nominal VR-VSC terminal DC voltage in kV.

Considering the small resistance of DC cables, a linearized form of (27) is obtained through Taylor Expansion as

$$V_{\mathrm{dcp}}^2-V_{\mathrm{dcp0}}^2\approx V_{\mathrm{dcv}}^2\left(1+\frac{2P_{\mathrm{p}}R_{\mathrm{dc}}}{V_{\mathrm{dcv}}^2}\right)-V_{\mathrm{dcv0}}^2\left(1+\frac{2P_{\mathrm{p0}}R_{\mathrm{dc}}}{V_{\mathrm{dcv0}}^2}\right) \quad (28)$$

$$V_{\mathrm{dcp}}^2-V_{\mathrm{dcp0}}^2\approx\left(V_{\mathrm{dcv}}^2-V_{\mathrm{dcv0}}^2\right)+2\left(P_{\mathrm{p}}-P_{\mathrm{p0}}\right) \quad (29)$$

As the active power change $(P_{\mathrm{p}}-P_{\mathrm{p0}})$ for the PR-VSC usually accounts for a relatively small percentage, thus equation (29) can be further simplified as

$$V_{\mathrm{dcp}}^2-V_{\mathrm{dcp0}}^2\approx\left(V_{\mathrm{dcv}}^2-V_{\mathrm{dcv0}}^2\right) \quad (30)$$

As observed in (30), the square of the DC voltage deviation at the PR-VSC terminal is approximately equal to that at the VR-VSC terminal, which further confirms that the DC voltage can be regarded as an intermediary to acquire frequency information of the VR-VSC connected AC Grid V.

Combining (26) and (30), the estimated frequency information of AC Grid V, f_{rv}, can be obtained as follows

$$f_{\mathrm{rv}}=\left(\frac{NC}{4S_{\mathrm{vsc}}H_{\mathrm{vscv}}}\left(V_{\mathrm{dcv}}^2-V_{\mathrm{dcv0}}^2\right)+1\right)f_0-\frac{H_{\mathrm{vscp}}\left(f_{\mathrm{p}}-f_0\right)}{H_{\mathrm{vscv}}} \quad (31)$$

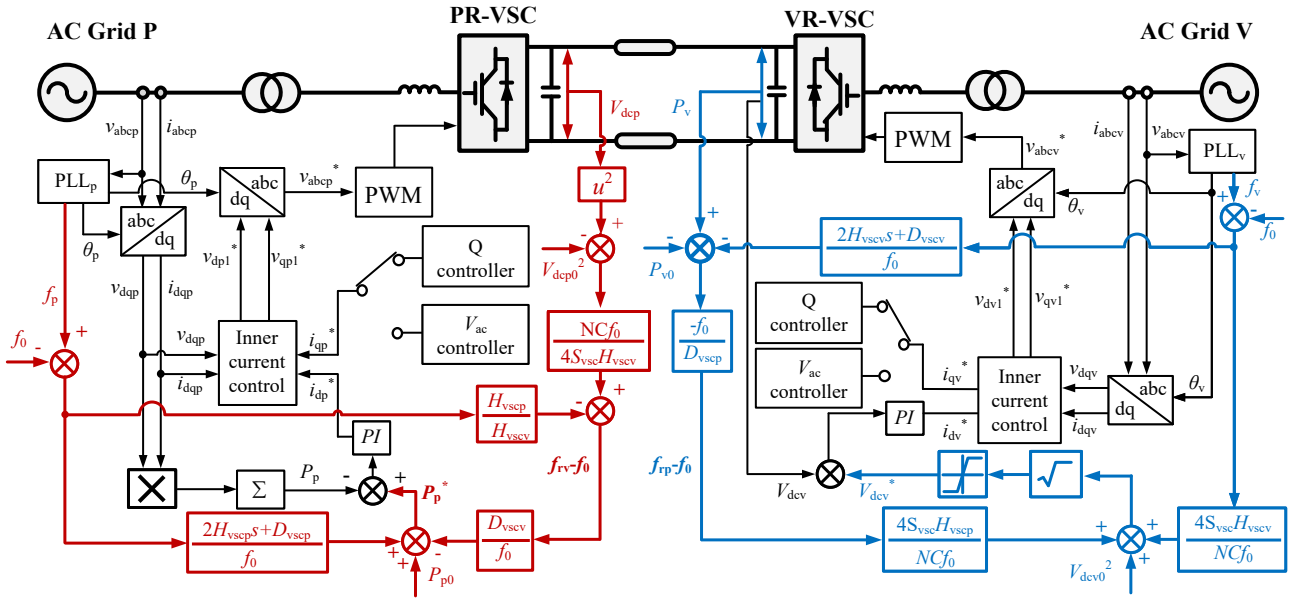

Fig. 5. The schematic diagram of the BIDE controller.

$$f_{\mathrm{rv}}-f_0=\frac{NC}{4S_{\mathrm{vsc}}H_{\mathrm{vscv}}}\left(V_{\mathrm{dcp}}^2-V_{\mathrm{dcp0}}^2\right)-\frac{H_{\mathrm{vscp}}\left(f_{\mathrm{p}}-f_0\right)}{H_{\mathrm{vscv}}} \quad (32)$$

It can be observed from (32) that the frequency information of the VR-VSC connected AC Grid V can be inferred at the PR-VSC locally by processing the PR-VSC terminal DC voltage without communication.

E. The complete BIDE algorithm and control implementation

To implement the communication-free BIDE algorithm in the VR-VSC control, the estimated AC Grid P frequency, f_{rp}, acquired by (24) replaces the corresponding frequency, f_{p}, in (12) to compute and update the DC voltage reference as

$$V_{\mathrm{v}}^*=\sqrt{V_{\mathrm{v0}}^2+\frac{4S_{\mathrm{vsc}}}{NCf_0}\left(H_{\mathrm{vscp}}\left(f_{\mathrm{rp}}-f_0\right)+H_{\mathrm{vscv}}\left(f_{\mathrm{v}}-f_0\right)\right)} \quad (33)$$

Similarly, in the PR-VSC control, the instantaneous AC Grid V frequency, f_{v}, in (18) is replaced by the estimated AC Grid V frequency, f_{rv}, acquired in (32) to compute and update the active power reference as

$$P_{\mathrm{v}}^*=P_{\mathrm{v0}}+\frac{2H_{\mathrm{vscp}}}{f_0}\frac{df_{\mathrm{p}}}{dt}+D_{\mathrm{vscp}}\frac{\left(f_{\mathrm{p}}-f_0\right)}{f_0}-D_{\mathrm{vscv}}\frac{\left(f_{\mathrm{rv}}-f_0\right)}{f_0} \quad (34)$$

Note that the nonlinear BIDE control scheme as designed in (33) and (34) are different from conventional linear droop controller which aims for power sharing purpose without achieving inertia emulation (e.g., a *P*-V_{DC}-*f* droop control scheme for a multi-terminal HVDC system [27]).

Fig. 5 illustrates the full implementation of BIDE in the VSC-HVSC control system, especially as highlighted in blue and red loops. The blue loop illustrates the inertia emulation control loops as described in (33), which can provide the inertial power bilaterally to the VSC-HVDC interconnected AC Grid P and AC Grid V. The AC Grid V frequency is measured locally by the VR-VSC's PLL$_2$, whereas the AC Grid P frequency deviation is estimated by processing the VR-VSC active power variations ΔP_{v} according to (24). The VR-VSC controller ultimately varies its terminal DC voltage reference in response to any frequency variation in AC Grid P or V according to (33) for bilateral inertial power provision.

The damping emulation control, as highlighted in the red loops of Fig. 5, is realized by modifying the PR-VSC active power reference. The AC Grid P frequency is measured locally by the PR-VSC's PLL$_1$ whereas the AC Grid V frequency deviation is estimated by processing the PR-VSC terminal DC voltage variations according to (32). Thus, the PR-VSC controller offsets its initial active power reference in response to any frequency variation in AC Grid P or V based on (34) to achieve the bilateral damping emulation.

F. DC capacitance selection

As can be seen in (33), a small DC capacitance can lead to large DC voltage deviations, whereas a large DC capacitance can lead to high capital cost. Therefore, the DC capacitance should be economically selected, while fulfilling the energy storage capacity required for the BIDE inertia emulation.

As analyzed in [25], the DC capacitance can be determined as

$$\begin{cases} C=H_0K_{\mathrm{vf}}\dfrac{2S_{\mathrm{vsc}}}{NV_{\mathrm{dc0}}f_0} \\ K_{\mathrm{vf}}=\max\left(\dfrac{f_{\max}-f_0}{V_{\mathrm{dcmax}}-V_{\mathrm{dc0}}},\dfrac{f_0-f_{\min}}{V_{\mathrm{dc0}}-V_{\mathrm{dcmin}}}\right) \end{cases} \quad (35)$$

where $f_{\max}$ and $f_{\min}$ are the upper and lower limits of frequency in Hz (e.g., $\pm$ 2.5 Hz [28]), respectively; V_{dcmax} and V_{dcmin} are the upper and lower limits of DC link voltage in kV (e.g., $\pm$ 0.15 pu [20]), respectively; and K_{vf} is the maximum ratio value of permitted frequency deviations by DC voltage deviations.

As shown in (35), the size of DC capacitance is proportional with the emulated inertia time constants H_{vscp} and H_{vscv} respectively. In other words, larger DC capacitance can provide more inertial power under the same RoCoF.

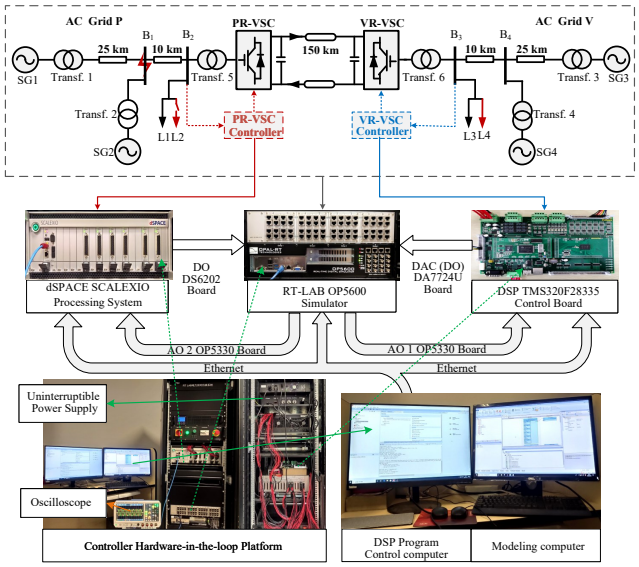

Fig. 6. Test system and experimental C-HIL platform.

When considering capacitor footprint, it can be significantly reduced by employing rapidly-developing supercapacitor technologies with high energy densities [29]. With respect to the cost for the proposed scheme, although one-off additional investment on capacitance augmentation is evitable, it can pay off in the longer term based on the service provisions of inertial and damping responses, which may be intensified by electricity markets [30] or imposed by system operators [31].

IV. Stability Analysis under The Proposed BIDE

To optimize the effects of the VSC-HVDC BIDE scheme on grid stability, modal analysis is carried out using a modified benchmark power system model of the two-area system [26] as shown in Fig. 6, where the interlinking AC double circuits of the two areas are replaced by a point to point VSC-HVDC system. All system parameters are presented in Table I.

A. Small-signal modelling of the studied system

The VSC-HVDC subsystem comprises three parts: 1) the AC filters and phase reactors; 2) the DC-link system; and 3) the VSC-HVDC control system. The two AC grids comprise two main parts: 1) the four SGs; and 2) the local AC networks. By interconnecting the inputs and outputs of the VSC-HVDC subsystem and the two AC grid subsystems, the small-signal model (SSM) can be obtained after linearization with the aid of the linear analysis tool in MATLAB/Simulink as

$$\begin{cases} \Delta\dot{\boldsymbol{X}} = \mathbf{A}\Delta\boldsymbol{X} + \mathbf{B}\Delta\boldsymbol{U} \\ \Delta\boldsymbol{Y} = \mathbf{C}\Delta\boldsymbol{X} + \mathbf{D}\Delta\boldsymbol{U} \end{cases} \tag{36}$$

where $\boldsymbol{X}$ is the state vector; $\boldsymbol{U}$ is the input vector; $\boldsymbol{Y}$ is the output vector; $\mathbf{A}$ is the state matrix; $\mathbf{B}$ is the input/control matrix; $\mathbf{C}$ is the output matrix; and $\mathbf{D}$ is the feedforward matrix. More modelling details can be found in [25], [32].

To validate the SSM, its step change responses are compared with those of the corresponding time-domain electromagnetic transient (EMT) model. The initial operating points are set at $[P_{\rm p}, V_{\rm dc}]$ = [0.7, 1] pu. The system dynamic responses under a step increase in the PR-VSC active power reference of 0.01 pu are presented in Fig. 7. It can be observed that the responses of the SSM are accurately aligned with those from the EMT model, verifying the correctness of the SSM.

TABLE I
Parameters of the VSC-HVDC system

Elements	Item	Value
VSC-HVDC station	Rated VSC power /MVA	300
	Nominal AC voltage /kV	300
	Nominal DC voltage /kV	±150
	Capacitance installed on each VSC /mF	7.5
	Reactor inductance /pu	0.15
	Reactor resistance /pu	0.005
VSC controller $K_{\rm p} + K_{\rm i}/s$	Outer power controller 1 ($K_{\rm p1}$, $K_{\rm Ii1}$)	0.4, 40
	Inner current controller 2 ($K_{\rm p2}$, $K_{\rm i2}$)	1, 100
	Outer DC voltage controller 1 ($K_{\rm p3}$, $K_{\rm i3}$)	1, 60
	Inner current controller 2 ($K_{\rm p4}$, $K_{\rm i4}$)	1, 200
	PLL ($K_{\rm ppll}$, $K_{\rm ipll}$)	60, 1400
Transformer	Rated ratios Transf.1∼Transf.4 /kV	230/13.8
	Rated ratios Transf.5∼Transf.6 /kV	230/150
	Rated power Transf.1∼Transf.6 /MVA	300
	Resistance /pu	0.002
	Leak inductance /pu	0.15
	Magnetization inductance /pu	500
AC cable	Resistance $r_{\rm a}$ / $\Omega\cdot{\rm m}^{-1}$	0.053
	Inductance $l_{\rm a}$ /H$\cdot{\rm m}^{-1}$	1.68e-4
	Capacitance $c_{\rm a}$ / F$\cdot{\rm m}^{-1}$	1.05e-8
DC cable	Resistance $r_{\rm d}$ /$\Omega\cdot{\rm m}^{-1}$	1.39e-2
	Inductance $l_{\rm d}$ /H$\cdot{\rm m}^{-1}$	1.59e-4
	Capacitance $c_{\rm d}$ /F$\cdot{\rm m}^{-1}$	2.31e-7
SG	Rated power SG1∼SG2 /MVA	300
	Rated power SG3∼SG4 /MVA	300
	Terminal voltage /kV	13.8
	Inertia time constant /s	3.2
	Damping factor	0
Governor	Turbine permanent droop $R_{\rm p}$/pu	0.05
	Turbine time constant $T_{\rm w}$/s	2.67
	Servo-motor time constant/s	0.07

B. Stability Margin Analysis

The system asymptotic stability is assessed by eigenvalue analysis. Figs. 8(a) and (b) present the root loci charts with the variations of inertia time constants $H_{\rm vscp}$ emulated by PR-VSC and $H_{\rm vscv}$ emulated by VR-VSC, respectively. Fig. 8(a) indicates the increase of $H_{\rm vscp}$ from 0.5 to 5.5 s moves the real part of the oscillation modes λ_1 and λ_2 close to the imaginary axis in the left plane with limited variation extent. Moreover, the increase of $H_{\rm vscp}$ moves the eigenvalues λ_3 and λ_4 away from the imaginary axis in the left plane, indicating an improved system stability with well-damped modes. Fig. 8(b) presents similar behaviors of the eigenvalue trajectories when increasing the emulated inertia time constant, $H_{\rm vscv}$.

Figs. 8(c) and (d) show the root loci charts during the variations of the emulated damping factors, $D_{\rm vscp}$ and $D_{\rm vscv}$, of PR-VSC and VR-VSC from 0.5 to 5.5 pu, respectively. Fig. 8(c) presents that the increase of emulated damping factors moves the eigenvalues λ_3 and λ_4 away from the real axis in the left plane with decreased damping, and moves the real pole λ_5 toward the imaginary axis leading to compromised

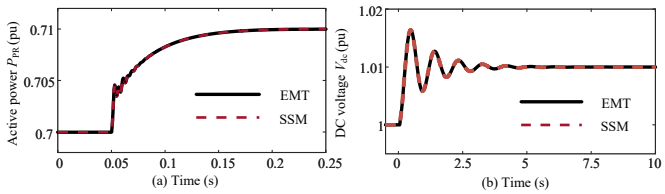

Fig. 7. Step response comparisons between the EMT model and SSM model: (a) 0.01pu step active power increase for PR-VSC; and (b) 0.01 pu step DC voltage increase for VR-VSC.

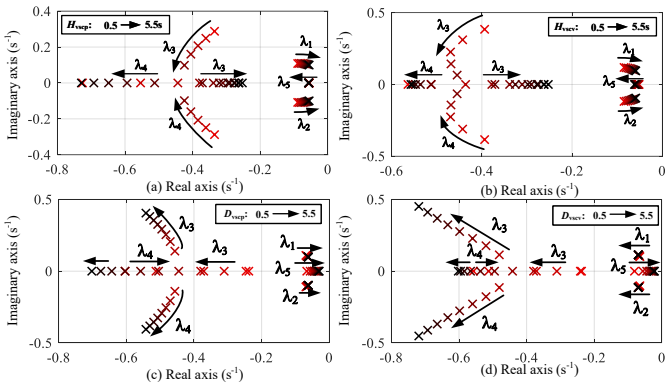

Fig. 8. Eigenvalue locus: (a) H_{vscp} varies from 0.5 $\sim$ 5.5 s; (b) H_{vscv} varies from 0.5 $\sim$ 5.5 s; (c) D_{vscp} varies from 0.5 $\sim$ 5.5 pu; and (d) D_{vscv} varies form 0.5 $\sim$ 5.5 pu;

stability, which indicates the damping factor should be chosen appropriately. Similar observations can also be found in Fig. 8(d) when varying D_{vscv}.

Based on the above analysis, both H_{vscp} and H_{vscv} are optimized at 3 s, and both D_{vscp} and D_{vscv} are optimized at 1 pu. These optimal values are adopted in the simulation evaluation of Section V. Stability comparisons of the proposed BIDE scheme to other inertia emulation schemes (e.g., the IDEC scheme in [10] and the CIDE scheme in [20]) can be potentially carried out in the future.

V. Simulation Evaluation

To verify the effectiveness of the proposed BIDE scheme, a C-HIL experimental platform is established as shown in Fig. 6. The platform consists of a dSPACE unit prototyping the PR-VSC BIDE controller, an external DSP-based programmable controller of TMS320F28335 prototyping the VR-VSC BIDE controller, and an RT-LAB OP5600 modelling the rest of the modified two-area system and the VSC-HVDC transmission circuits using HYPERSIM toolbox in MATLAB/Simulink.

As shown in Fig. 6, AC Grid P and V both comprise of two static loads and two SGs. The SGs are modelled in a seventh-order state space with IEEE standard parameters [33]. For AC Grid P, the initial active power generation of SG1 and SG2 are both 200 MW. For AC Grid V, the initial active power generation of SG3 and SG4 are both 100 MW. The fixed static load L1 is S_{L1} = P_{L1} + jQ_{L1} = 200 - j20 MW. The switchable load L2 is S_{L2} = P_{L2} + jQ_{L2} = 20 - j12 MW, accounting for 10 % of the total load in AC Grid P. In AC Grid V, the fixed static load L3 is S_{L3} = P_{L3} + jQ_{L3} = 400 + j50 MW. The switchable load L4 is S_{L4} = P_{L4} + jQ_{L4} = 20 + j2.5 MW, accounting for 5 % of the total load in AC Grid V.

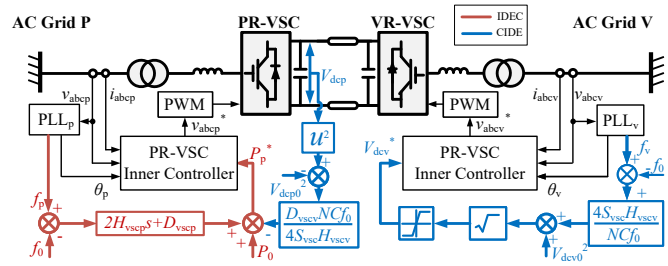

Fig. 9. The conventional CIDC controller for simulation comparisons

The performances of three different schemes as introduced in Section I are compared as follows

1) The BIDE scheme proposed in this paper, which provides bilateral inertial power from DC capacitance and bilateral damping power to both the interconnected grids, with the parameter settings of H_{vscp} = 3 s, H_{vscv} = 3 s, D_{vscp} = 1 pu and D_{vscv} = 1 pu based on the stability analysis in Section IV.

2) The CIDC scheme defined as the combined version of IDEC and CIDE in this paper, as shown in Fig. 9, which implements the IDEC scheme reported in [19] on PR-VSC as highlighted in red and the CIDE scheme proposed in [25] on VR-VSC as highlighted in blue, with the parameter settings of H_{vscp} = 3 s, H_{vscv} = 3 s, D_{vscp} = 1 pu and D_{vscv} = 1 pu.

3) The TC scheme as introduced in [34], which provides neither inertial power nor damping power to either AC grid, with the parameter settings of H_{vscp} = 0 s, H_{vscv} = 0 s, D_{vscp} = 0 pu and D_{vscv} = 0 pu.

Other controller parameters (e.g., the cascaded PI controllers and the PLLs) are selected the same as shown in Table I.

Three grid events are simulated: *A.* step load increase in AC Grid P; *B.* step load decrease in AC Grid V; and *C.* grid fault in AC Grid P.

A. Step load increase in AC Grid P

Load L2 is switched in at t = 5 s in AC Grid P and the system dynamics are illustrated in Fig. 10. The frequency f_{p} and RoCoF df_{p}/dt of AC Grid P, as shown in Figs. 10(a) and (c), both exhibit significant reduction in the first peaks under BIDE and CIDC. However, unlike BIDE, the power for the inertial and damping provision by CIDC both comes from AC Grid V, which results in a larger frequency deviation and a larger RoCoF in AC Grid V, as shown in Figs. 10(b) and (d). It is worthy notice that there is a steady-state frequency deviation 0.004 Hz in AC Grid V at t = 90 s under BIDE due to the damping provision from AC Grid V. The inertial power under BIDE is released by varying the DC voltage based on (33) within $\pm$ 0.04 pu, as shown in Fig. 10(e). Fig. 10(f) shows the frequencies f_{p} of AC Grid P and f_{v} of AC Grid V can be accurately estimated for PR-VSC and VR-VSC based on (24) and (32), respectively. Although BIDE and CIDC provide similar inertial and damping power to AC Grid P, as observed in Fig. 10(g), CIDC causes larger power variations at AC Grid V as shown in Fig. 10(h), and consequently, larger SG3 power output fluctuations as presented in Fig. 10(j). For simplification, only one SG in each AC grid is presented as both SGs have similar dynamics.

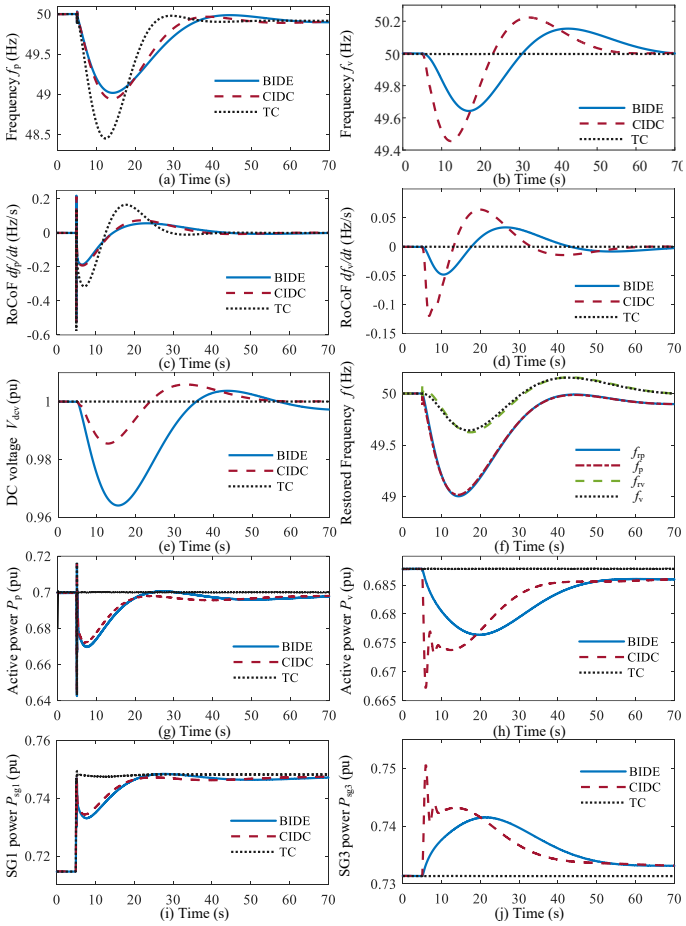

Fig. 10. Step load increase response: (a) frequency f_{p}; (b) frequency f_{v}; (c) RoCoF df_{p}/dt; (d) RoCoF df_{v}/dt; (e) DC voltage V_{dcv}; (f) restored frequency f_{rp} and f_{rv}; (g) active power P_{p}; (h) active power P_{v}; (i) SG1 power P_{sg1}; and (j) SG3 power P_{sg3}.

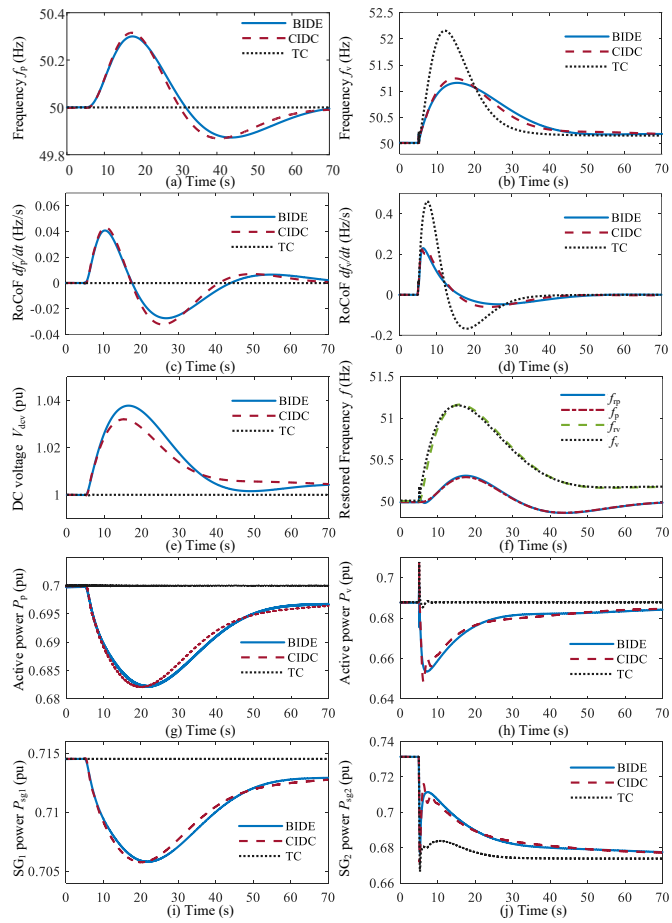

Fig. 11. Step load decrease response: (a) frequency f_{p}; (b) frequency f_{v}; (c) RoCoF df_{p}/dt; (d) RoCoF df_{v}/dt; (e) DC voltage V_{dcv}; (f) restored frequency f_{rp} and f_{rv}; (g) active power P_{p}; (h) active power P_{v}; (i) SG1 power P_{sg1}; and (j) SG3 power P_{sg3}.

On the other hand, TC cannot provide the inertial and damping power to mitigate the transient power imbalance in AC Grid P. Therefore, the transmitted power of the VSC-HVDC system maintains constant, as observed in Figs. 10(g) and (h). As a result, larger frequency deviations and RoCoF occur in AC Grid P as shown in Figs. 10(a) and (c), compared to BIDE and CIDC. In addition, the steep power change in SG1 at the beginning of the load increase as seen in Fig. 10(i), may increase its out-of-step risk. Such a risk can be more serious when AC Grid P is a weak grid with higher RES penetration.

B. Step load decrease in AC Grid V

Fig. 11 presents the system dynamics when load L4 is switched out at t = 5 s. As presented in Figs. 11(b) and (d), both BIDE and CIDC effectively suppress the frequency deviations and RoCoF of AC Grid V as they both act to increase the DC voltage, as shown in Fig. 11(e), for releasing the capacitance power to emulate inertia time constant based on (33). The instantaneous frequencies f_{rp} of AC Grid P and f_{rv} of AC Grid V can also be accurately acquired at PR-VSC and VR-VSC respectively, and the corresponding results are compared to the real frequencies, f_{p} and f_{v}, measured by the PLLs as shown in Fig. 11(f). Figs. 11(g) and (i) show that there are apparent active power changes in SG1 and PR-VSC under both BIDE and CIDC, which provide the damping power and support AC Grid V via the VSC-HVDC link. It is worthy noticing that the inertial energy for AC Grid P comes from the augmented DC capacitance under the BIDE scheme rather than from the AC Grid V, avoiding exacerbating AC Grid V power imbalances as shown in Fig. 11(b). Note that BIDE and CIDC provide similar inertial and damping power to AC Grid V, but BIDE can also effectively damp the power oscillations of VR-VSC and SG3, as evident in Figs. 11(h) and (j), respectively.

On the other hand, TC scheme cannot provide the inertial and damping power to AC Grid V and the output power of PR-VSC and VR-VSC remain constant, as shown in Figs. 11(g) and (h), respectively. This results in a larger frequency deviation and a larger RoCoF in AC Grid V, as shown in Figs. 11(b) and (d), and larger power variations of SG3, as shown in Fig. 11(j).

C. Three-phase grid faults

Fig. 12 illustrates the performances of three control schemes under a 140 ms three-phase remote fault at bus B_1 in AC Grid P from t = 1 s, which results in a significant 0.6 pu voltage drop, as shown in Fig. 12(a). The DC voltage is varied by the BIDE and CIDC schemes to release the inertial power as shown in Fig. 12(b). As can be generally observed in Figs. 12(c) and

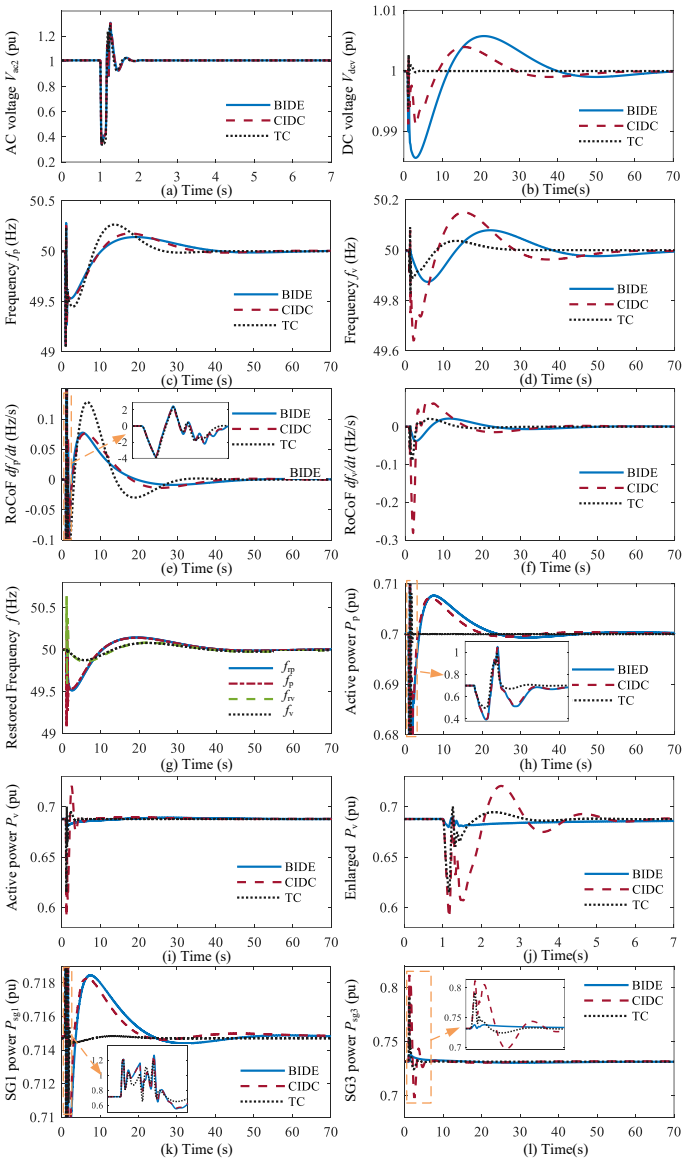

Fig. 12. The system response for 140 ms three-phase ground faults: (a) AC voltage amplitude V_{ac2}; (b) DC voltage V_{dcv}; (c) frequency f_{p}; (d) frequency f_{v}; (e) RoCoF df_{p}/dt; (f) RoCoF df_{v}/dt; (g) restored frequency f_{rp} and f_{rv}; (h) active power P_{p}; (i) active power P_{v}; (j) enlarged figure of (i); (k) SG1 power P_{sg1}; and (l) SG3 power P_{sg3}.

(d), when compared to TC, BIDE can significantly underpin the faulted AC grid by providing inertial and damping responses, sacrificing a trivial amount of frequency variation in the remote AC Grid V. CIDC achieves a similar frequency stabilizing effect, but the frequency variation magnitude and RoCoF in the remote AC grid are higher than BIDE as observed in Figs. 12(d) and (f). Fig. 12(g) shows the accuracies of the estimated frequency information of AC Grid P and V are affected at the beginning of the fault due to the steep variations in the PR-VSC active power and the DC voltage as shown in Figs. 12(i) and (b), but are improved when the fault is cleared. Fig. 12(h) shows the PR-VSC active power is varied to provide the inertial and damping power when the fault is cleared. Figs. 12(i), (j) and (l) clearly show that VR-VSC and SG3 experience more active power oscillations under the CIDC scheme compared to the proposed BIDE scheme as the inertial power for AC Grid P is directly provided from the AC Grid V.

As can be seen in the results in Section *V.A*, *V.B* and *V.C*, compared to the CIDC scheme, the BIDE scheme proposed in this paper can effectively provide bilateral inertial power from DC capacitance and bilateral damping power to both interconnected AC grids.

VI. Conclusion

This paper proposes a bilateral inertia and damping emulation (BIDE) control scheme for VSC-HVDC transmission systems to autonomously underpin frequency stability for interconnected asynchronous AC grids. The inertia emulation is realized by varying the DC capacitance energy via the DC voltage regulating VSC, whereas the damping emulation is achieved by coordinating the active power flow via the power regulating VSC.

In contrast to the other historically-reported schemes which only support for one side of the grid, the proposed BIDE scheme has the following features: 1) instantaneous inertial response can be bilaterally provided to interconnected AC grids, with flexibly-defined inertia time constants; 2) the SG damping effects can be flexibly emulated and bilaterally provided for both AC grids; 3) the inertial and damping support can be "simultaneously" provided to both connected asynchronous grids without priority discrimination; and 4) communication is avoided, as the grid frequencies can be precisely extracted from locally measured DC voltage and active power variations.

Various simulation studies verify that the VSC-HVDC system under BIDE can interact with the two interconnected AC grids, minimize grid frequency deviations, and reduce angular oscillations under different grid contingencies. In the future, it is important to equip VSC-HVDC systems with BIDE, as grid inertia and system damping will inevitably decline due to the rapid replacement of conventional synchronous generations by inertia- and damping-less RESs.

References

[1] J. Dutton and M. Lockwood, "Ideas, institutions and interests in the politics of cross-border electricity interconnection: Greenlink, Britain and Ireland," *Energy Policy*, vol. 105, pp. 375–385, 2017.

[2] Z. Liu, G. Chen, X. Guan, Q. Wang, and W. He, "A concept discussion on northeast asia power grid interconnection," *CSEE J. of Power Energy Syst.*, vol. 2, no. 4, pp. 87–93, 2016.

[3] J. Zhu, J. M. Guerrero, W. Hung, C. D. Booth, and G. P. Adam, "Generic inertia emulation controller for multi-terminal voltage-source-converter high voltage direct current systems," *IET Renew. Power Gener.*, vol. 8, no. 7, pp. 740–748, 2014.

[4] "Black system south australia 28 september 2016," Australian Energy Market Operator (AEMO), Mar. 2017. [Online]. Available: https://apo.org.au/node/74886.

[5] "Technical report on the events of 9 august2019," National Grid UK, Sept. 2019. [Online]. Available: https://www.ofgem.gov.uk/sites/default/files/docs/2019/09/eso_technical_report_-_final.pdf.

[6] R. G. de Almeida and J. A. Pecas Lopes, "Participation of doubly fed induction wind generators in system frequency regulation," *IEEE Trans. Power Syst.*, vol. 22, no. 3, pp. 944–950, 2007.

[7] Y. Su, H. Li, Y. Cui, S. You, Y. Ma, J. Wang, and Y. Liu, "An adaptive PV frequency control strategy based on real-time inertia estimation," *IEEE Trans. Smart Grid*, vol. 12, no. 3, pp. 2355–2364, 2020.

[8] J. Zhu, J. Hu, W. Hung, C. Wang, X. Zhang, S. Bu, Q. Li, H. Urdal, and C. D. Booth, "Synthetic inertia control strategy for doubly fed induction generator wind turbine generators using lithium-ion supercapacitors," *IEEE Trans. Energy Convers.*, vol. 33, no. 2, pp. 773–783, 2017.

[9] L. Zhang, L. Harnefors, and H.-P. Nee, "Power-synchronization control of grid-connected voltage-source converters," *IEEE Trans. Power Syst.*, vol. 25, no. 2, pp. 809–820, 2009.

[10] Q.-C. Zhong and G. Weiss, "Synchronverters: Inverters that mimic synchronous generators," *IEEE Trans. Ind. Electron.*, vol. 58, no. 4, pp. 1259–1267, 2010.

[11] Q.-C. Zhong, "Virtual synchronous machines: A unified interface for grid integration," *IEEE Power Electron. Mag.*, vol. 3, no. 4, pp. 18–27, 2016.

[12] M. Guan, W. Pan, J. Zhang, Q. Hao, J. Cheng, and X. Zheng, "Synchronous generator emulation control strategy for voltage source converter (VSC) stations," *IEEE Trans. Power Syst.*, vol. 30, no. 6, pp. 3093–3101, 2015.

[13] M. Chen, D. Zhou, and F. Blaabjerg, "Modelling, implementation, and assessment of virtual synchronous generator in power systems," *J. Modern Power Syst. and Clean Energy*, vol. 8, no. 3, pp. 399–411, 2020.

[14] P. Rodriguez, I. Candela, and A. Luna, "Control of PV generation systems using the synchronous power controller," in *2013 IEEE Energy Conversion Congress and Exposition*. IEEE, 2013, pp. 993–998.

[15] W. Zhang, A. M. Cantarellas, J. Rocabert, A. Luna, and P. Rodriguez, "Synchronous power controller with flexible droop characteristics for renewable power generation systems," *IEEE Trans. Sustain. Energy*, vol. 7, no. 4, pp. 1572–1582, 2016.

[16] W. Zhang, A. Tarraso, J. Rocabert, A. Luna, J. I. Candela, and P. Rodriguez, "Frequency support properties of the synchronous power control for grid-connected converters," *IEEE Trans. Industry Appl.*, vol. 55, no. 5, pp. 5178–5189, 2019.

[17] Y. Phulpin, "Communication-free inertia and frequency control for wind generators connected by an HVDC-link," *IEEE Trans. Power Syst.*, vol. 27, no. 2, pp. 1136–1137, 2011.

[18] M. Kabsha and Z. H. Rather, "A new control scheme for fast frequency support from HVDC connected offshore wind farm in low-inertia system," *IEEE Trans. Sustain. Energy*, vol. 11, no. 3, pp. 1829–1837, 2019.

[19] J. Zhu, X. Wang, J. Zhao, L. Yu, S. Li, Y. Li, J. M. Guerrero, and C. Wang, "Inertia emulation and fast frequency-droop control strategy of a point-to-point VSC-HVDC transmission system for asynchronous grid interconnection," *IEEE Trans. Power Electron.*, vol. 37, no. 6, pp. 6530–6543, 2022.

[20] J. Zhu, C. D. Booth, G. P. Adam, A. J. Roscoe, and C. G. Bright, "Inertia emulation control strategy for VSC-HVDC transmission systems," *IEEE Trans. Power Syst.*, vol. 28, no. 2, pp. 1277–1287, 2012.

[21] Z. Shen, J. Zhu, L. Ge, S. Bu, J. Zhao, C. Y. Chung, X. Li, and C. Wang, "Variable-inertia emulation control scheme for VSC-HVDC transmission systems," *IEEE Trans. Power Syst.*, vol. 37, no. 1, pp. 629–639, 2022.

[22] H. Liu and Z. Chen, "Contribution of VSC-HVDC to frequency regulation of power systems with offshore wind generation," *IEEE Trans. Energy Convers.*, vol. 30, no. 3, pp. 918–926, 2015.

[23] Y. Li, Z. Xu, J. Østergaard, and D. J. Hill, "Coordinated control strategies for offshore wind farm integration via VSC-HVDC for system frequency support," *IEEE Trans. Energy Convers.*, vol. 32, no. 3, pp. 843–856, 2017.

[24] Y. Xiong, W. Yao, J. Wen, S. Lin, X. Ai, J. Fang, J. Wen, and S. Cheng, "Two-level combined control scheme of VSC-MTDC integrated offshore wind farms for onshore system frequency support," *IEEE Trans. Power Syst.*, vol. 36, no. 1, pp. 781–792, 2020.

[25] J. Zhu, Z. Shen, S. Bu, X. Li, C. D. Booth, W. Qiu, H. Jia, and C. Wang, "Coordinated flexible damping mechanism with inertia emulation capability for MMC-MTDC transmission systems," *IEEE J. Emerg. Sel. Topics Power Electron.*, vol. 9, no. 6, pp. 7329–7342, 2021.

[26] P. Kundar, *Power system stability and control*. New York, NY, USA: McGraw-Hill, 1994.

[27] Y. Li, S. Liu, J. Zhu, X. Yuan, Z. Xu, and K. Jia, "Novel MTDC droop scheme with decoupled power control for enhancing frequency stabilities of weak AC systems," *IET Renewable Power Generation*, vol. 14, no. 11, pp. 2007–2016, 2020.

[28] "The Grid Code—Issue 6, Revision 12," National Grid UK, Mar. 2022. [Online]. Available: https://www.nationalgrideso.com/document/162271/download.

[29] G. Mandic, A. Nasiri, E. Ghotbi, and E. Muljadi, "Lithium-ion capacitor energy storage integrated with variable speed wind turbines for power smoothing," *IEEE J. Emerg. Sel. Topics Power Electron.*, vol. 1, no. 4, pp. 287–295, 2013.

[30] F. Sioshansi, *Consumer, prosumer, prosumager: How service innovations will disrupt the utility business model*. Academic Press, 2019.

[31] "Network code on operational security," ENTSO-e, July 2015. [Online]. Available: https://eepublicdownloads.entsoe.eu/clean-documents/pre2015/resources/OS_NC/130924-AS-NC_OS_2nd_Edition_final.pdf.

[32] G. O. Kalcon, G. P. Adam, O. Anaya-Lara, S. Lo, and K. Uhlen, "Small-signal stability analysis of multi-terminal VSC-based DC transmission systems," *IEEE Trans. Power Syst.*, vol. 27, no. 4, pp. 1818–1830, 2012.

[33] F. Demello, R. Koessler, J. Agee, P. Anderson, J. Doudna, J. Fish, P. Hamm, P. Kundur, D. Lee, G. Rogers *et al.*, "Hydraulic-turbine and turbine control-models for system dynamic studies," *IEEE Trans. Power Syst.*, vol. 7, no. 1, pp. 167–179, 1992.

[34] D. Kong and X.-P. Zhang, "Modelling and control of offshore wind farm with VSC-HVDC transmission system," in *9th IET International Conference on AC and DC Power Transmission (ACDC 2010)*. IET, 2010, pp. 1–6.